JOURNAL OF GUIDANCE, CONTROL, AND DYNAMICS
Vol. 31, No. 4, July–August 2008

# Fuel-Efficient Interferometric Imaging Maneuvers in Near-Earth Orbit

Jaime Ramirez* and Suman Chakravorty†
*Texas A&M University, College Station, Texas 77843-3134*

DOI: 10.2514/1.27555

**In this paper, a methodology to design fuel-efficient maneuvers for space-based interferometric imaging systems located in near-Earth orbits, under time and imaging constraints, is proposed. The methodology is hierarchical and consists of a higher-level nonlinear programming problem and a lower-level linear quadratic tracker. Solutions are obtained for the purpose of quantifying the relationship between the quality of an image obtained by a multispacecraft interferometric imaging system and the dynamic requirements of such imaging maneuvers. These maneuvers are then used for the design of a system capable of obtaining very-high-resolution images from a near-Earth orbital location. To relate the fuel requirements with image quality, the relationship between the imaging process and the error in the final image is studied, and a quality factor is designed to relate the reliability of an image to the trajectory of the spacecraft and, hence, the fuel usage. As an application, a midinfrared imager system located at geostationary orbit is studied and features of the design of such maneuvers are enumerated.**

## Nomenclature

| | | |
|---|---|---|
| $A_{\text{tel}}$ | = | area of the telescopes |
| $a$ | = | orbital rate of the circular orbit in the CW equations |
| $a_r$ | = | radial acceleration |
| $\bar{a}_r = a_r/(\mathrm{d}r/\mathrm{d}t)$ | = | rate of change of the radial velocity with respect to the radius |
| $a_t$ | = | tangential acceleration |
| $\bar{a}_t = a_t/(\mathrm{d}r/\mathrm{d}t)$ | = | rate of change of the tangential velocity with respect to the radius |
| $d_{\text{pix}}$ | = | resolution of the image |
| $e(\nu)$ | = | error in the frequency content |
| $e_\nu$ | = | energy of the photons at frequency $\nu$ |
| $h$ | = | Planck's constant |
| $I(\nu)$ | = | actual frequency content |
| $\hat{I}(\nu)$ | = | estimation of the image frequency content |
| $\hat{I}_o(\nu)$ | = | measurements of the frequency content |
| $I_{p\text{th}}$ | = | value of the threshold for the intensity of error-bounded pixels |
| $J$ | = | mutual coherence measurements |
| $K$ | = | upper bound on the spiral rate $\frac{\mathrm{d}r}{\mathrm{d}\theta}$ |
| $M$ | = | number of collectors |
| $\mathcal{M}(\nu)$ | = | modulation transfer function |
| $\mathcal{N}(\nu)$ | = | noise |
| $n_{\text{pix}}$ | = | number of pixels in an image |
| $n_s$ | = | density number of photons |
| $p_{\max}$ | = | maximum value for the probability of an image to have an error greater than the bound |
| $R_f$ | = | final radius of the maneuver |
| $r$ | = | radial position of the spacecraft in the spiral maneuver |
| $T$ | = | total time of the maneuver |
| $T_{\max}$ | = | maximum time allowed to finish the imaging maneuver |
| $T_{\text{opt}}$ | = | temperature of the optics |
| $u_x, u_y, u_z$ | = | controls in the $x$, $y$, and $z$ directions |
| $v_r$ | = | radial velocity |
| $v_t$ | = | tangential velocity |
| $x, y, z$ | = | standard CW coordinates |
| $\bar{z}$ | = | approximate distance to the target |
| $\alpha_i$ | = | proportionality constants for the relative distance between spacecraft pairs |
| $\beta_i$ | = | constants defining the multiplicity of the coverage disks |
| $\Delta r_{nm}$ | = | projection in the observation plane of the relative position of spacecraft $n$ and $m$ |
| $\Delta\lambda$ | = | bandwidth of the detection |
| $\delta A$ | = | area of the collectors |
| $\delta J$ | = | random term in the mutual coherence measurements |
| $\delta T$ | = | time of collection for one measurement |
| $\epsilon$ | = | fractional transmission of thermal energy |
| $\eta$ | = | absorption coefficient of the atmosphere |
| $\lambda$ | = | wavelength of the signal |
| $\mu_{\text{tot}}$ | = | rate of photons per second |
| $\nu$ | = | two-dimensional frequency vector |
| $\xi$ | = | emissivity coefficient of the radiating body |
| $\rho$ | = | size of the coverage disks in the $u$–$v$ plane |
| $\sigma^2(x)$ | = | variance of $x$ |
| $\varsigma$ | = | optical efficiency of the elements |
| $\tau_{\text{opt}}$ | = | optical efficiency of the detector |
| $\Phi = 1/v_r(\alpha_m r)$ | = | discretized optimization variable |
| $\|\cdot\|$ | = | standard Euclidean norm |
| $\|\cdot\|_\infty$ | = | infinity norm |

Received 28 August 2006; revision received 21 August 2007; accepted for publication 3 September 2007. 

*Graduate Student Researcher, Aerospace Engineering, 611 B, Harvey R. Bright Building.

†Assistant Professor, Aerospace Engineering, 611 B, Harvey R. Bright Building.

## I. Introduction

THE motivation for this research is the design of multispacecraft interferometric imaging systems (MSIIS) located in a near-Earth orbit. An interferometric imaging system is a sparse aperture interferometric system that allows for the synthesis of a large-size aperture through the combination of the signal from several subapertures, allowing for the formation of images with resolution that is orders of magnitude better than that of a single telescope [1].

Interferometric imaging falls under the category of long baseline interferometry [2] that was first developed in the context of synthetic aperture radars (SAR) and has been successfully used in Earth-based astronomy [3]. The use of spacecraft formations for this purpose has been proposed, and previous literature has dealt with the definition of

the optical requirements and capacities of interferometric imaging systems aiming to obtain astronomical images, specifically, the imaging of extrasolar planets [4–6]. Different techniques of interferometry using formations of separated spacecraft have been proposed, and their application to space-based targets have been studied [5,7].

At the same time, the technical drawbacks of the optics of such systems are being overcome due to the improvement of computational systems and the development of technologies that allow better signal reception (resulting in higher signal-to-noise ratio) and less stringent requirements in position and metrology accuracy [8]. On the other hand, the dynamics and control of multispacecraft systems in orbital configurations have been topics of considerable research, allowing for the design of robust and accurate trajectory control systems [5,9]. Furthermore, the development of high specific impulse thrust systems has reduced the technical difficulties for satellite formations performing active tasks. However, the relationship between the dynamic requirements of the spacecraft in a formation and the imaging quality in active interferometric imaging tasks is far from being well studied.

Previous formation designs optimize the locations of the constituent telescopes such that some metric of image quality is optimized [10,11]. These correspond to static optimization problems. However, for an MSIIS, due to the higher-resolution requirements, the design variables are the trajectories of the constituent spacecraft. To assess the minimum requirements of these trajectories, an optimization problem has to be posed.

In previous work, the dynamics of the spacecraft have been related to the modulation transfer function (MTF) of the optical system, and time/fuel optimal problems have been posed [4,12–15]. In a previous paper by the authors, a heuristic approach considered the design of minimum fuel trajectories in the subset of spirals, subject to deep-space dynamics, for an exosolar planet imaging application [16]. However, when the corresponding problem is posed for formations in a near-Earth orbit, the decoupled structure of the dynamic equations breaks down and other desirable features of the optimization problem, such as convexity, disappear. Thus, the structure of the problem does not allow for the design of a computationally efficient optimization method for the exact problem. Additionally, new optical and kinematic constraints arise that are different from those studied in previous research [4]. In this paper, the fuel optimization problem is posed for an interferometric imaging system subject to the dynamic constraints in a near-Earth circular orbit. To find fuel-efficient trajectories, a methodology is proposed that designs trajectories subject to Clohessy–Wiltshire (CW) dynamic equations while satisfying the image-quality constraint. The methodology has a hierarchical structure in which an outer loop optimizes the fuel usage of the spacecraft system subject to deep-space dynamics, whereas a linear quadratic regulator (LQR) inner-loop controller is used to track the trajectories generated by the outer loop.

To evaluate the applicability of the method, a midinfrared system located at geostationary orbit (GEO), with a resolution capacity of 1 m for targets emitting thermal radiation on the Earth's surface, is studied. A midinfrared system can give appropriate information that cannot be found by imaging in visible light, such as temperatures of buildings and hot spots where engines or machinery could be hidden. It also allows one to see through haze, smoke, and dust, and is capable of detecting human bodies and allows for night images. A telescope located at a geostationary orbit able to acquire images in the infrared (IR) frequency range with a resolution close to 1 m would require an aperture of hundreds of meters, and, thus, a single monolithic telescope or even a large-scale space structure is infeasible in such an application.

The paper is organized as follows. In Sec II, the interferometric imaging maneuvers are reviewed, and spiral maneuvers are introduced as a solution for the trajectory optimization problem. In Sec. III, a review of interferometry is given, and a relationship between the trajectories of the spacecraft and the noise in the image is developed. In Sec. IV, the criteria for the quality of an image are introduced and related to the variance of the error in the imaging process. In Sec. V, the solution algorithm is presented. In Sec. VI, the results of some simulations for different cases are given to study the feasibility and characteristics of such systems.

## II. Multispacecraft Interferometric Imaging Systems

An MSIIS consists of a group of telescopes carried on individual spacecraft, acting in concert to synthesize a larger optical aperture. By interfering the light acquired by every pair of spacecraft, a coverage of the $u$–$v$ plane is attained, and by reconstructing the frequency content of an image, it is possible to generate an image of the target.

The total observed frequency content is

$$\hat{I}_o(\nu) = \mathcal{M}(\nu) I(\nu) + \mathcal{N}(\nu) \tag{1}$$

where $I(\nu)$ is the actual intensity at the spatial frequency $\nu$, and $\mathcal{N}(\nu)$ is the noise that corrupts those measurements.

The MTF $\mathcal{M}(\nu)$ is a transfer function characteristic of the synthesized instrument. This function is composed by the contributions of every combination of telescope pairs over the time of the maneuver and relates the frequency content of the actual image to the observed image. It can be calculated from the telemetry of the trajectories of the spacecraft and allows to calculate an estimate of the frequency plane image $\hat{I}(\nu)$ at frequency points where $\mathcal{M}$ is different from zero:

$$\hat{I}(\nu) = \mathcal{M}^{-1}(\nu) \hat{I}_o(\nu) \tag{2}$$

Then

$$\hat{I}(\nu) = I(\nu) + e(\nu) \tag{3}$$

where $I(\nu)$ is the actual image, and the error $e$ is

$$e(\nu) = \frac{\mathcal{N}(\nu)}{\mathcal{M}(\nu)} \tag{4}$$

In previous work [4,12,17], the expressions for the MTF $\mathcal{M}$, the noise $\mathcal{N}$, and consequently the error $e$ for multispacecraft interferometric imaging systems have been derived as functions of the spacecraft trajectories and are given by

$$\mathcal{M}(\nu) = \sum_{m=1}^{M} \sum_{n=1}^{M} \int_0^T \hat{A}_p \left( \nu - \frac{\Delta r_{mn}(t)}{\lambda \bar{z}} \right) \mathrm{d}t \tag{5}$$

and

$$\mathcal{N}(\nu) = \frac{1}{\hat{I}_{\text{est}}} \sum_{m=1}^{M} \sum_{n=1}^{M} \int_0^T \delta J_{mn} \hat{A}_p \left( \nu - \frac{\Delta r_{mn}(t)}{\lambda \bar{z}} \right) e^{-j\psi_{mn}(t)} \mathrm{d}t \tag{6}$$

where $\hat{I}_{\text{est}}$ is the total intensity of radiation at the observation plane, $T$ is the total time of maneuver, $\Delta r_{nm}$ is the projection of the relative position of the $n$ and $m$ spacecraft in the plane perpendicular to the optical axis, $\lambda$ is the detected light wavelength, $\bar{z}$ is the distance to the target, $\delta J_{mn}$ is a Gaussian distributed random variable that represents the error in the mutual intensity measurement between the $m$th and the $n$th spacecraft, whose variance $\sigma^2(\delta J_{mn})$ depends on the type of interferometric process, and $\hat{A}_p$ is the aperture function in the observation plane. The term $\psi_{mn}$ represents a phasing factor that is dependent on the positions of the $m$th and $n$th spacecraft on the image plane. See [4] for additional details. This error can be assumed to be uniform over all spacecraft pairs on the imaging plane and will be represented in the following as $\delta J$.

Considering the random nature of the light emission process and the central limit theorem, given that the image is composed of a large number of independent measurements, an expression for the variance of the error at any point in the spatial frequency plane $\nu$ is found to be [4,18]

$$\sigma^2(e(\nu)) = \frac{\sigma^2(\delta J)\delta T}{\hat{I}^2_{\text{est}} \int_0^T \sum_n \sum_m \hat{A}_p(\nu - \frac{\Delta r_{mn}}{\lambda z})\, \mathrm{d}t} \tag{7}$$

If the variance of the error is bounded above by $\sigma^2_{e\max}$, a constraint on the spacecraft trajectory can be obtained as

$$\sum_m^M \sum_n^M \int_0^T \hat{A}_p\left(\nu - \frac{\Delta r_{mn}}{\lambda z}\right) \mathrm{d}t \geq \bar{\Delta} \tag{8}$$

with

$$\bar{\Delta} = \frac{\sigma^2(\delta J)\delta T}{\hat{I}^2_{\text{est}}\sigma^2_{e\max}} \tag{9}$$

In the preceding equations, the nature of the multispacecraft acquisition process is revealed: each pair of telescopes contributes to the formation of the image with an instantaneous transfer function, and the addition of every combination of telescope pairs over the total time of the maneuver forms the total transfer function of the synthesized optical system. The instantaneous transfer function depends on the aperture function in the observation plane, $\hat{A}_p$, which accounts for the finiteness of the telescopes. For the purpose of this work, the function $\hat{A}_p$ can be approximated by a value of unity within a circle of radius $\rho$ and zero elsewhere, that is,

$$\hat{A}_p(x) = \begin{cases} 1 & \text{if } \|x\| \leq \rho \\ 0 & \text{otherwise} \end{cases}$$

Respectively, the variance of the error is inversely proportional to the accumulated time of coverage for a given frequency $\nu$ [integral in Eq. (8)] and, thus, covering every region of the $u$–$v$ plane for an accumulated time longer than a given bound, assures a minimum value of the variance of the frequency content error.

Then the imaging problem consists of finding the trajectories of the spacecraft such that the disks defined by the $u$–$v$ support function cover each point on the $u$–$v$ plane for a minimum given amount of time for the acquisition of enough information (photons) at every point inside the coverage region. This is illustrated in the simulation in Fig. 1, in which the reconstruction of images is given for two different cases. In the first one, every region of the support in the $u$–$v$ plane is covered long enough such that the variance of the error $\sigma^2[e]$ is low for every point. In the other case, all the support of the frequency plane is also covered, but in this case some regions are appropriately covered, whereas others are covered for a shorter amount of time, the error is greater, and, hence, the image is not reconstructed with the required accuracy. Notice that in the second image, even if the noise in the inner and outer regions is much smaller than in the first image, having a poorly covered region reduces the quality. Thus, for satisfactory image formation, active control of the spacecraft is required to allow for complete and appropriate coverage of the $u$–$v$ plane. A spiral maneuver is a convenient choice. Spiral maneuvers have been shown to be time optimal [13]; they define an optimization problem to solve for the spacecraft trajectories, as well as allow for rotation of the optical axis to aim at different targets and reorganization in case of the failure of an individual or a collection of spacecraft. The coverage of the $u$–$v$ plane by a spiral maneuver is shown in Fig. 2.

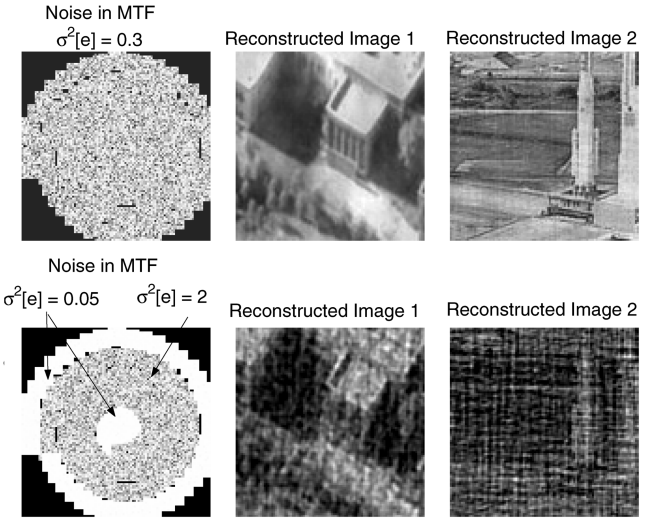


**Fig. 1 A comparison of two reconstructed images for different coverages in the $u$–$v$ plane.**

In the subset of spiral maneuvers, an optimization problem can be posed subject to dynamic constraints, the time constraint, and two coverage constraints: full-paint constraint (FPC) and expansion-rate constraint [15].

The FPC refers to the constraint that the total time of coverage of any given region of the frequency plane needs to be greater than a prespecified lower bound. In a symmetric spiral maneuver, the coverage disks are arranged in concentric rings whose radii are in a fixed ratio with respect to each other, and these ratios are determined by the polygonal geometry of the formation. This results in $N_R$ concentric spirals of coverage in the frequency plane that expand at different rates, as seen in Fig. 2. For instance, in the six spacecraft cases in the figure, there are three concentric rings of coverage disks, and the ratios of the rings with respect to the innermost ring is always $\alpha = \sqrt{3}$ and $\alpha_3 = 2$, where $\alpha_i$ refers to the proportionality constant for the $i$th ring. Note that due to the highly constrained geometry of the formation, the radial expansion rate of any of the rings is completely specified by that of the inner ring and the constants $\alpha_i$. Also, the number of coverage disks at any point in the plane is either 1 or 2 depending on the geometry. In the preceding case, the two inner rings each have two coverage disks at every point of instantaneous coverage in the $u$–$v$ plane, whereas the outermost ring has one coverage disk. This coverage multiplicity is denoted by $\beta_i$, where $i$ refers to the $i$th ring.

Heuristically, the time of coverage of an annular portion of the frequency plane is equal to the summation of the time spent by each one of the concentric expanding spirals in that region. Given the geometrical relationship between the expansion rate of each spiral and the radial velocity of the spacecraft, the FPC can be written as a function of the radial velocity at the various radial positions [4,14,16] (however, the details of the derivation are nontrivial and can be found in Proposition 7.1.1 in [4] and Proposition 2 in [14]):

$$\sum_i^{N_R} \alpha_i \beta_i [1/v_r(\alpha_i r/\alpha_{N_R})] \geq r\bar{\bar{\Delta}} \tag{10}$$

where

$$\bar{\bar{\Delta}} = \frac{2\bar{\Delta}}{\rho^2 M}$$

$v_r(\cdot)$ is the radial velocity of the coverage disks in the innermost ring, $\alpha_i$ is the ratio of the radius of the $i$th ring of coverage disks to the innermost ring of coverage disks (i.e., $\alpha_1 = 1$), and $\beta_i \in \{1, 2\}$ are binary valued constants that define the multiplicity of the coverage disks in ring $i$ and depend on whether the total number of spacecraft is odd or even (see [19] for details).

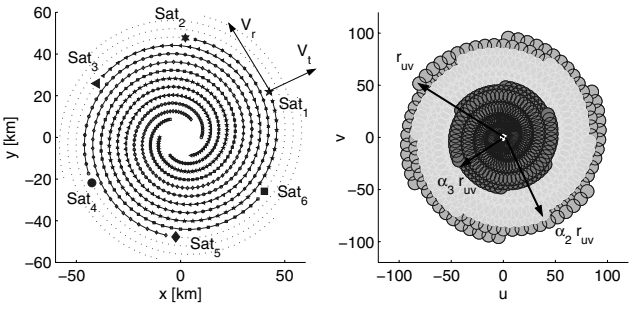


**Fig. 2 The $u$–$v$ plane coverage in spiral maneuvers.**

Additionally, the rate of expansion of the spiral $k = \mathrm{d}r/\mathrm{d}\theta$ has to be bounded to prevent gaps between successive turns of the spiral. Its maximum value depends on the size and angular separation between the disks in the $u$–$v$ plane, which are dependent on the number and size of the telescopes. Noting that

$$\frac{\mathrm{d}r}{\mathrm{d}\theta} = \frac{\mathrm{d}r/\mathrm{d}t}{\mathrm{d}\theta/\mathrm{d}t}$$

and that

$$\frac{\mathrm{d}\theta}{\mathrm{d}t} = \frac{v_t}{r}$$

this constraint is written as Eq. (13).

Given that the radius is a monotonically increasing function of time, defining $r$ as the independent variable, under the two preceding coverage constraints and under time and dynamic constraints, the fuel optimal spiral trajectory problem can then be posed as [12]

$$\min_{v_r, v_t} \int_0^{R_f} \sqrt{\bar{a}_r^2 + \bar{a}_t^2}\, \mathrm{d}r \tag{11}$$

subject to

$$\sum_i^{N_R} \alpha_i \beta_i \frac{1}{v_r\left(\frac{\alpha_i r}{\alpha_{N_R}}\right)} \geq r\bar{\bar{\Delta}}, \quad \forall\ r \in [0, R_f] \tag{12}$$

$$\frac{r v_r(r)}{v_t(r)} \leq K \tag{13}$$

$$a_r' = f_r(r, v_r, v_t) \tag{14}$$

$$a_t' = f_t(r, v_r, v_t) \tag{15}$$

$$a_r^2 + a_t^2 \leq A_{\max}^2 \tag{16}$$

$$\int_0^{R_f} \frac{\mathrm{d}r}{v_r(r)} \leq T_{\max} \tag{17}$$

where the radial and tangential velocities rates of change

$$\bar{a}_r = a_r \Big/ \frac{\mathrm{d}r}{\mathrm{d}t}, \qquad \bar{a}_t = a_t \Big/ \frac{\mathrm{d}r}{\mathrm{d}t}$$

are functions of the radius, $R_f$ is the final radius of the maneuver, $T_{\max}$ is an upper boundary for the time of the maneuver, and $K$ is the upper boundary for the expansion rate previously described. The cost function is the integral of the required accelerations throughout the maneuver, the constraints in Eqs. (12) and (13) are coverage constraints, Eqs. (14–16) are dynamic constraints, and Eq. (17) is the time constraint.

This problem, then, is to find a pair of variables $v_r$, $v_t$, or, equivalently, $v_r$, $k$ [since $k = f(v_r, v_t)$] as functions of the radial position of the spiral and, thus, defining the geometry and kinematics of the spiral.

## III. Error Variance in Interferometric Process

In this section, the relationship between the error in the interferometric process and the dynamics of the multispacecraft interferometric system for different types of interferometric methods are described.

### A. Direct Interferometry

In a direct interferometer, the light from the two spacecraft is directed to a combiner and interfered, and the amplitude and phase of the peak in the interfered signal is measured, giving the information of amplitude and phase of the mutual coherence of the source at the relative positions of the spacecraft. The variance in error of the mutual coherence $J$ between a pair of detectors is given by [3,12]

$$\sigma^2[\delta J_{nm}] = \left(1 + \frac{1-\epsilon}{\tau_{\text{opt}} n_s (e^{h\nu/kT_{\text{opt}}} - 1)}\right) \frac{\tau_{\text{opt}} e_\nu I_{\text{est}}}{M \delta A \delta T} \tag{18}$$

where $\epsilon$ is the fractional transmission of thermal energy, $T_{\text{opt}}$ is the temperature of the optics, $\tau_{\text{opt}}$ is the optical efficiency of the detector given the losses in the transfer optics, $n_s$ is the density number of photons, $e_\nu$ is the energy of photons at frequency $\nu$, and $M$ is the number of collectors. Thus, $M\delta A$ is the area of collection, $h$ is Planck's constant, and $\delta T$ is the time of collection. In direct interferometry, the signal cannot be amplified or manipulated to compensate the optical effects of the mirrors that affect the total signal for the process. It has to be divided to interfere with the light of every other telescope and so the final signal is divided by $(M-1)$. A term accounting for the optical efficiency $\varsigma$ also has to be included [6]. Then, the parameter $\bar{\Delta}$ in Eq. (9) for this case can be written as

$$\bar{\Delta} = \left(1 + \frac{1-\epsilon}{\tau_{\text{opt}} n_s (e^{h\nu/kT_{\text{opt}}} - 1)}\right) \frac{(M-1)^2}{\tau_{\text{opt}} \varsigma \mu_{\text{tot}} \sigma_{\max}^2[e(\nu)]} \tag{19}$$

where $\mu_{\text{tot}}$ is the total rate of photons per second arriving at the observation plane.

### B. Entry Pupil: Heterodyne and Intensity Interferometry

Heterodyne and intensity interferometry are affected by the uncertainty principle noise, which is different from the noise in a direct detection system [6]. In heterodyne interferometry, the acquired signal is first interfered with a coherent signal from the local oscillator (LO) that allows reproducing a downlinked version of the acquired signal in the radio frequency wavelength. A signal in the radio frequency band can be transmitted, manipulated, and later interfered offline, and so there is no need to have a combiner to directly interfere the light from the source and the signal can be compensated by the losses in the optics. Intensity interferometry uses the method developed for the Hanbury–Brown–Twiss interferometer, obtaining the mutual coherence intensity from the second-order variations of the signal. However, these two methods introduce the uncertainty noise on the signal. For practical purposes, the noise and signal of intensity interferometry behave similarly to the heterodyne interferometric process. The noise variance of this method can be written as [6]

$$\sigma^2[\delta J_{nm}] = \left(1 + \frac{1}{n_s} + \frac{1-\epsilon}{n_s (e^{h\nu/kT_{\text{opt}}} - 1)}\right) \frac{e_\nu I_{\text{est}}}{M \delta A \delta T} \tag{20}$$

Following a similar reasoning, the parameter in Eq. (9) for entry pupil multispacecraft interferometry is found to be

$$\bar{\Delta} = \left(1 + \frac{1}{n_s} + \frac{1-\epsilon}{n_s (e^{h\nu/kT_{\text{opt}}} - 1)}\right) \frac{1}{\mu_{\text{tot}} \sigma_{\max}^2[e(\nu)]} \tag{21}$$

Notice the difference with direct interferometry. The term $n_s$ is an important factor differentiating the two cases. This term is caused by the uncertainty principle noise induced in the entry pupil process. The value of $n_s$ for a thermal source is given by

$$n_s = \frac{1}{e^{h\nu/kT} - 1} \tag{22}$$

For the temperatures of a body on Earth, this value is much smaller than 1 and decreases with the frequency. Also, the factor derived from the division of the signal and optical efficiency coefficients are not present in heterodyne interferometry, making it more suitable for cases with a larger number of spacecraft.

In this section, the parameter $\bar{\Delta}$ has been defined; thus, the FPC constraint Eq. (12) can be set to define a fuel minimization problem that will attain a bounded error level in the frequency content of the image.

## IV. Reliability of the Image

To calculate the required minimum time of coverage for a maneuver, it is preferable to define a maximum value for the variance of the frequency content error $\sigma^2_{\max}[e]$. In this section, two criteria are defined, relating the reliability of the image to the variance of the error in the $u$–$v$ plane. One is defining a pixelwise reliability, that is, defining a limit in the probability of error for any pixel of the image. The second is defining a quality requirement as a restriction in the probability of the total error of the image (summation of the squared error of each pixel).

### A. Pixelwise Bound

A requirement of a bound in the error of any point $I_j(x) \geq I_{p\text{th}}$, $I_j(x) \in I(x)$ is

$$\text{Prob}\{|I(x) - \hat{I}(x)| \geq kI_{\text{pth}}\} \leq p_{\max}\rho \tag{23}$$

that is,

$$\text{Prob}\{|\tilde{F}_j(I(\nu)) - \tilde{F}_j(\hat{I}(\nu))| \geq kI_{\text{pth}}\} \leq p_{\max} \tag{24}$$

for any value of $j$, where $I(\nu)$ is a vector with the frequency information of the image, and the $j$th point of the image is

$$I_j(x) = \tilde{F}_j(I) = v_j^T H^* I \tag{25}$$

where

$$I(x) = H^* I(\nu) \tag{26}$$

$H^*$ being the inverse Fourier transform, a linear operator that in the discrete case can be defined by the matrix components

$$h^*_{i,j} = \frac{1}{\sqrt{n_{\text{pix}}}}\omega^{(i-1)(j-1)} \tag{27}$$

$$\omega = e^{\imath 2\pi\Delta r_{xy}/(\lambda z)} \tag{28}$$

and

$$v_j^T = (0, 0, \ldots, 1, \ldots, 0, 0) \tag{29}$$

a vector that extracts the value of the $j$th pixel from an image formed by $n_{\text{pix}}$ pixels. $kI_{p\text{th}}$ is a maximum value for the error pixelwise, such that every pixel in the actual image with an intensity greater than $I_{p\text{th}}$ will have a bounded error. For any point $j$,

$$|\tilde{F}_j(I(\nu)) - \tilde{F}_j(\hat{I}(\nu))|^2 = |v_j^T H^*(I - \hat{I}(\nu))|^2 \tag{30}$$

$$= |(I(\nu) - \hat{I}(\nu))^* H v_j v_j^T H^*(I(\nu) - \hat{I}(\nu))| \tag{31}$$

and

$$v_j^T H^* = H_j^* \tag{32}$$

$$H v_j = H_j \tag{33}$$

$H_j$ being the $j$th column of the matrix $H$ and $H_j^*$ being the $j$th row of the matrix $H^*$. Then

$$E[|\tilde{F}_j(I(\nu)) - \tilde{F}_j(\hat{I}(\nu))|^2] = E[|(I(\nu) - \hat{I}(\nu))^* H_j H_j^*(I(\nu) - \hat{I}(\nu))|] \tag{34}$$

$$= E[|H_j^*(I(\nu) - \hat{I}(\nu))(I(\nu) - \hat{I}(\nu))^* H_j|] \tag{35}$$

$$= H_j^* E[|(I(\nu) - \hat{I}(\nu))(I(\nu) - \hat{I}(\nu))^*|] H_j \tag{36}$$

$$= H_j^* R_e H_j \tag{37}$$

where $R_e$ is the covariance matrix for the error on the image in the frequency plane and can be considered diagonal because the measurements in the frequency plane are uncorrelated. Thus,

$$E[|\tilde{F}_j(I) - \tilde{F}_j(\hat{I})|^2] = \sum_i h^*_{ij} h_{ij} E[|e_i|]^2 \tag{38}$$

where $e_i$ is the error in the $i$th component of the image in the frequency plane. Because the operator $H$ is unitary and endowed with a special structure, it follows that

$$h^*_{ij} h_{ij} = \frac{1}{n_{\text{pix}}}$$

and then

$$E[|\tilde{F}_j(I) - \tilde{F}_j(\hat{I})|^2] = \frac{1}{n_{\text{pix}}}\|e\|_2^2 \tag{39}$$

where $\|e\|_2$ is the mean squared error $(\sum_i E|e_i|^2)^{1/2}$. Defining the worst-case error as $\|e\|_\infty = (\max_i\{E|e_i|^2\})^{1/2}$, it follows that

$$\|e\|_\infty^2 \geq \frac{\|e\|_2^2}{n_{\text{pix}}}$$

and, thus,

$$E[|\tilde{F}_j(I) - \tilde{F}_j(\hat{I})|^2] \leq (\max_i\{E|e_i|^2\}) \tag{40}$$

The preceding inequality relates the error in the $j$th pixel of the image to the error in the spatial frequency content of the image.

The function $\tilde{F}$ is a linear transformation of $e$, and $e$ is a Gaussian distributed variable; then $\tilde{F}(e)$ is a zero mean Gaussian distributed variable and Eq. (23) is satisfied if

$$\sigma^2[e_i] \leq \frac{1}{Q} \tag{41}$$

where

$$Q = \frac{2n_{\text{pix}}(erf^{-1}(1 - p_{\max}))^2}{k^2 I^2_{p\text{th}}} \tag{42}$$

### B. Chi Squared: Total Error Bound

A bound for the total error in the image can be defined by

$$\text{Prob}\left\{\sum |I(x) - \hat{I}(x)|^2 \geq K\right\} \leq p_{\max} \tag{43}$$

Given Parseval's theorem [1], the preceding condition becomes

$$\text{Prob}\left\{\sum |I(\nu) - \hat{I}(\nu)|^2 \geq K\right\} \leq p_{\max} \tag{44}$$

Now, defining the complex normal distributed variable

$$x = \frac{\text{Re}(I_j - \hat{I}_j)}{\sqrt{E|\text{Re}(I_j - \hat{I}_j)|^2}} + i\frac{\text{Im}(I_j - \hat{I}_j)}{\sqrt{E|\text{Im}(I_j - \hat{I}_j)|^2}} \sim N(0,1) + iN(0,1) \tag{45}$$

and given the acquisition process, the real and imaginary parts are identically distributed random variables. Then

$$x = \frac{\mathrm{Re}(I_j - \hat{I}_j) + i\mathrm{Im}(I_j - \hat{I}_j)}{\sqrt{E|\mathrm{Re}(I_j - \hat{I}_j)|^2}} \sim N(0,1) + iN(0,1) \tag{46}$$

such that

$$\chi^2 = \sum_{i=0}^{r-1} x^2 \tag{47}$$

is a chi-square distributed variable with $r$ degrees of freedom, where $r = 2n_{\mathrm{pix}}$. Then, if $\sigma_p$ is the solution for the equation

$$1 - \mathcal{G}_r\left(\frac{K}{\sigma_p^2}\right) = p_{\max} \tag{48}$$

where

$$\mathcal{G}_r(y) = \frac{\gamma(r/2, y/2)}{\Gamma(r/2)} \tag{49}$$

and $\gamma$, $\Gamma$ are incomplete and complete gamma functions, respectively, and if

$$\mathrm{Prob}\left\{\chi^2 \le \left(\frac{K}{\sigma_p^2}\right)\right\} = p_{\max} \tag{50}$$

and

$$\sum |I - \hat{I}|^2 \le \sigma_p^2 \chi^2 \tag{51}$$

$$\sum |I - \hat{I}|^2 \le \sigma_p^2 \sum_{j=0}^{r-1} \frac{|I_j - \hat{I}_j|^2}{E[|\mathrm{Re}(I_j - \hat{I}_j)|^2]} \tag{52}$$

that is, if

$$\sum_{j=0}^{r-1} \frac{|I_j - \hat{I}_j|^2}{\sigma_p^2} \le \sum_{j=0}^{r-1} \frac{|I_j - \hat{I}_j|^2}{E|\mathrm{Re}(e(v_j))|^2} \tag{53}$$

then

$$\mathrm{Prob}\left\{\sum |I - \hat{I}|^2 \ge K\right\} \le p_{\max} \tag{54}$$

The quality condition is then given by Eq. (53), which describes the hypercone defined by the intersection of a hyperellipsoid with the hypersphere given by the left side of Eq. (53). If all the axes of the hyperellipsoid are restricted to be inside the hypersphere, the reliability of the image is guaranteed. Then, a solution for Eq. (53) that satisfies the error requirement is

$$\sigma^2[e_i] \le \frac{1}{Q} \tag{55}$$

where

$$Q = \frac{\mathcal{G}_r^{-1}(1 - p_{\max})}{K} \tag{56}$$

Thus, a parameter $Q$ has been defined that is directly related to the quality of the image. Figure 3 shows the same image for different levels of quality $Q$, along with its total error $K$ and pixelwise error distribution $k$.

By arguments of ergodicity, the distribution over the ensemble is assumed equivalent to the distribution of the measurements over time. Then, a relationship between $k$ (the quality), $p_{\max}$ (the probability of getting an error worse than that), and the trajectories of the spacecraft has thus been defined. Figure 4 shows $Q$ as a function of the error probability for different $k$ (the pixelwise quality) for different probabilities, and Fig. 5a shows $Q$ as a function of $K$ (the total error quality) for different values of $p_{\max}$ (notice that it is basically constant). Figure 5b shows the quality index $Q$ as the value of $K$ is increased.

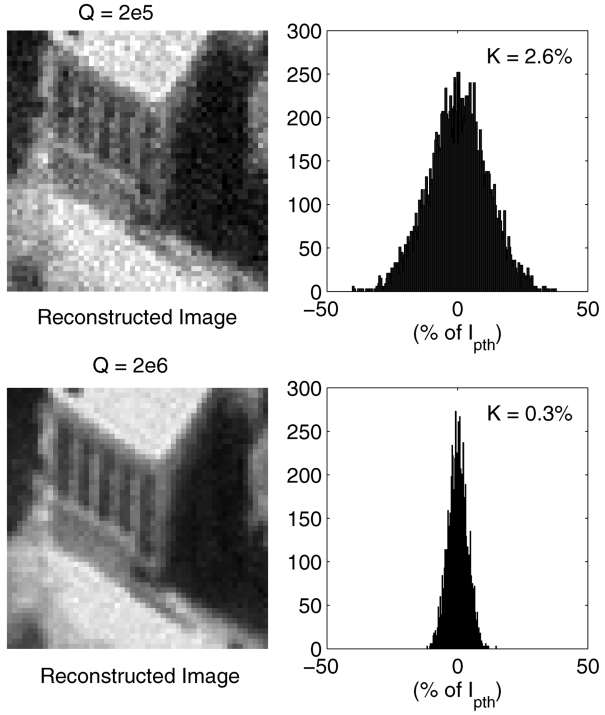


**Fig. 3 The quality index of the image. The right side plot displays the error distribution of the pixels and the total error value $K$.**

## V. Near-Minimum Fuel Maneuvers

In this section, a solution algorithm is proposed to calculate near-minimum fuel trajectories to acquire knowledge about the upper bounds of the system. The system is considered to be subject to CW dynamic equations.

It is intended to find solutions for the optimization problem [Eqs. (8–14)]. The problem has been solved for deep-space dynamics [16], but the symmetry used to solve the problem for that case is lost for the case of CW dynamics:

$$\ddot{x} - 2a\dot{y} - 3a^2 x = u_x \tag{57}$$

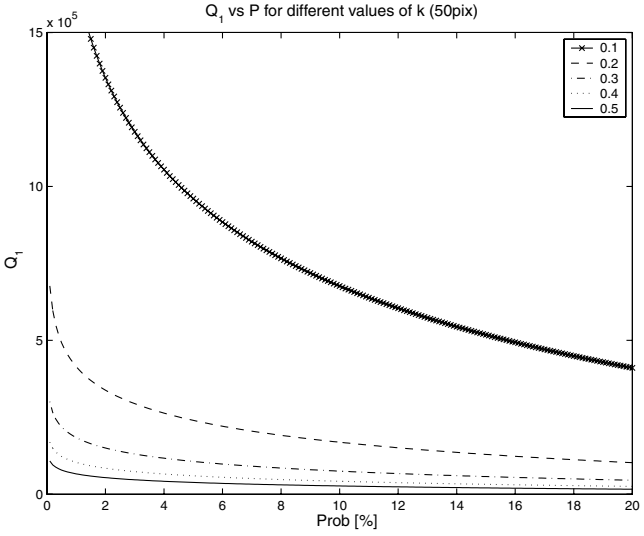


**Fig. 4 The pixelwise quality vs error probability for different $k$.**

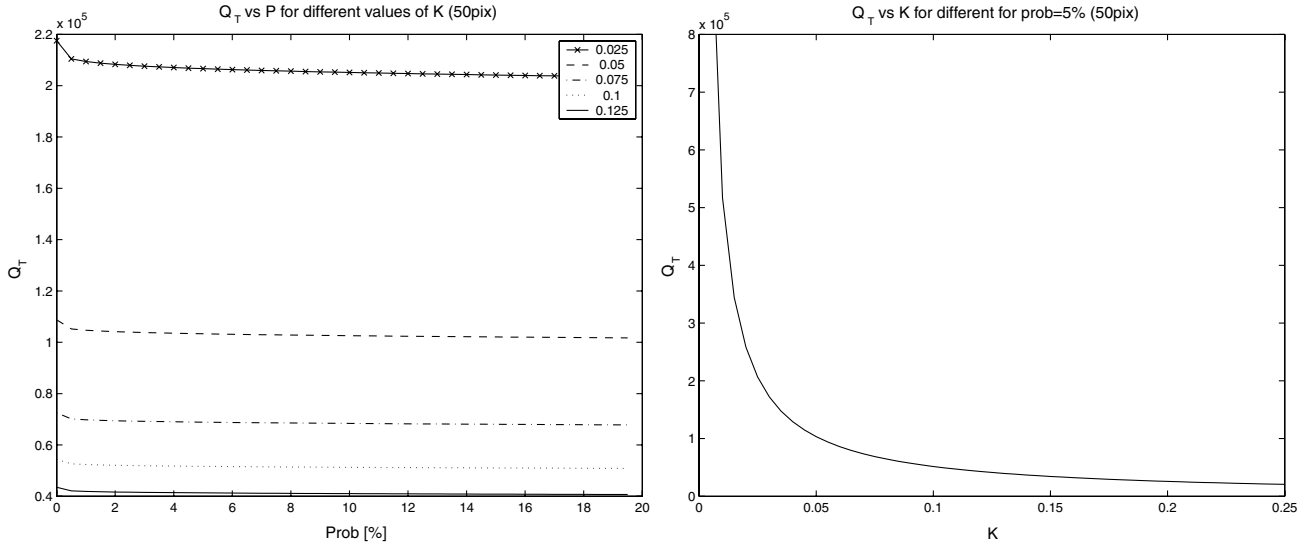


a) b)

**Fig. 5 a) The total quality vs error probability for different $K$; b) the total quality vs $K$, given error probability.**

$$\ddot{y} + 2a\dot{x} = u_y \tag{58}$$

$$\ddot{z} + a^2 z = u_z \tag{59}$$

where $a$ is the orbital rate, and $x$, $y$, and $z$ are the standard local-vertical–local-horizontal (LVLH) coordinates. Therefore, the cost function not only depends on the radial and tangential components of the velocities in the spiral, but is also dependent on the trajectory of each individual spacecraft. Solving this optimization problem requires a solution for the trajectories of the spacecraft in three-dimensional space subject to asymmetric dynamics. The solution for such a problem would require a highly time-consuming computational method as the fuel optimization problem does not possess any desirable optimization characteristic, the number of variables is increasingly large, and it is not a convex problem.

A near-minimum fuel solution for the problem is proposed assuming that the total cost of the maneuver for the $M$ spacecraft is optimized by dividing the problem into two subproblems. First, the spacecraft maneuvers are optimized assuming deep-space dynamics, that is, a nonperturbed double integrator. Next, the resulting trajectories are tracked under CW dynamics using a linear quadratic optimal control that applies constraints in the projections of the trajectories perpendicular to the optical axis and defines trajectories that achieve the desired coverage. In previous work [16], the process in which the optimization problem stated in Eqs. (11–17) converted to a fuel optimization process for deep-space dynamics has been considered. In that case, the independent variable is the radius of the maneuver and the problem consists of finding $v_r(r)$ and $k(r)$, which minimize the fuel cost function:

$$J = \int_0^{R_{\max}} \frac{v_r(r)}{k^2} \sqrt{r^2 + 4k^2}\, \mathrm{d}r \tag{60}$$

Under the assumption that the maximum rate of expansion of the spiral is optimal, the problem is reduced to find $v_r(r)$, the radial velocity as a function of the radius. The previously stated problem is solved considering the discretized optimization variable

$$\Phi_i = \Phi(r_i) \qquad i = 1, \ldots, N \tag{61}$$

$$\Phi(r) = \frac{1}{v_r(\alpha_{N_R} r)} \tag{62}$$

which allows stating a convex nonlinear programming (NLP) problem

$$\min \sum_{i=1}^{N} \frac{1}{\Phi_i} \cdot \frac{\sqrt{r_i^2 + 4k_i^2}}{k_i^2} \tag{63}$$

subject to

$$\Gamma \cdot \Phi \geq r\bar{\bar{\Delta}} \tag{64}$$

$$\alpha_N \delta r \|\Phi\|_1 \leq T_{\max} \tag{65}$$

$$\Phi_i^2 \geq \frac{\sqrt{r_i^2 + 4k_i^2}}{k_i^2 A_{\max}} \tag{66}$$

where

$$\|\Phi\|_1 = \sum_i = 1^N \Phi_i$$

$\delta r$ is the discretization step in $r$, and

$$\Gamma = \sum_{i=1}^{N_R} \alpha_i \beta_i \mathcal{W}_{(\alpha_i/\alpha_{N_R})} \tag{67}$$

being the matrix $\mathcal{W}_\alpha$, a contraction matrix, that is the approximation in discrete space of the operator

$$\mathcal{F}_\alpha(\Phi(r)) = \Phi(\alpha r) \tag{68}$$

which has the form

$$\Phi(\alpha r) = \mathcal{W}_\alpha \cdot \Phi(r) \tag{69}$$

$$= \begin{bmatrix} 1 & 0 & \cdots & 0 & 0 & \cdots & 0 & 0 \\ 0 & \cdots & 0 & p & 1-p & 0 & \cdots & 0 \\ & & & \cdots & & & & \\ 0 & \cdots & 0 & 0 & 0 & 0 & 0 & 1 \\ 0 & 0 & 0 & 0 & 0 & 0 & 0 & 0 \\ & & & \cdots & & & & \\ 0 & 0 & 0 & 0 & 0 & 0 & 0 & 0 \end{bmatrix} \begin{bmatrix} \Phi(r_i) \\ \Phi(r_{i+1}) \\ \cdots \\ \cdots \\ \cdots \\ \Phi(r_{n_s-1}) \\ \Phi(r_{n_s}) \end{bmatrix} \tag{70}$$

where $p$ is a proportionality constant that calculates the value of $\Phi$ at the point $\alpha r$, as the linear interpolant of $\Phi(r_{i-1})$ and $\Phi(r_i)$. As a particular case, $\mathcal{W}_1$ is the identity matrix. This nonlinear problem has been shown to be convex [18], and a sequential quadratic algorithm

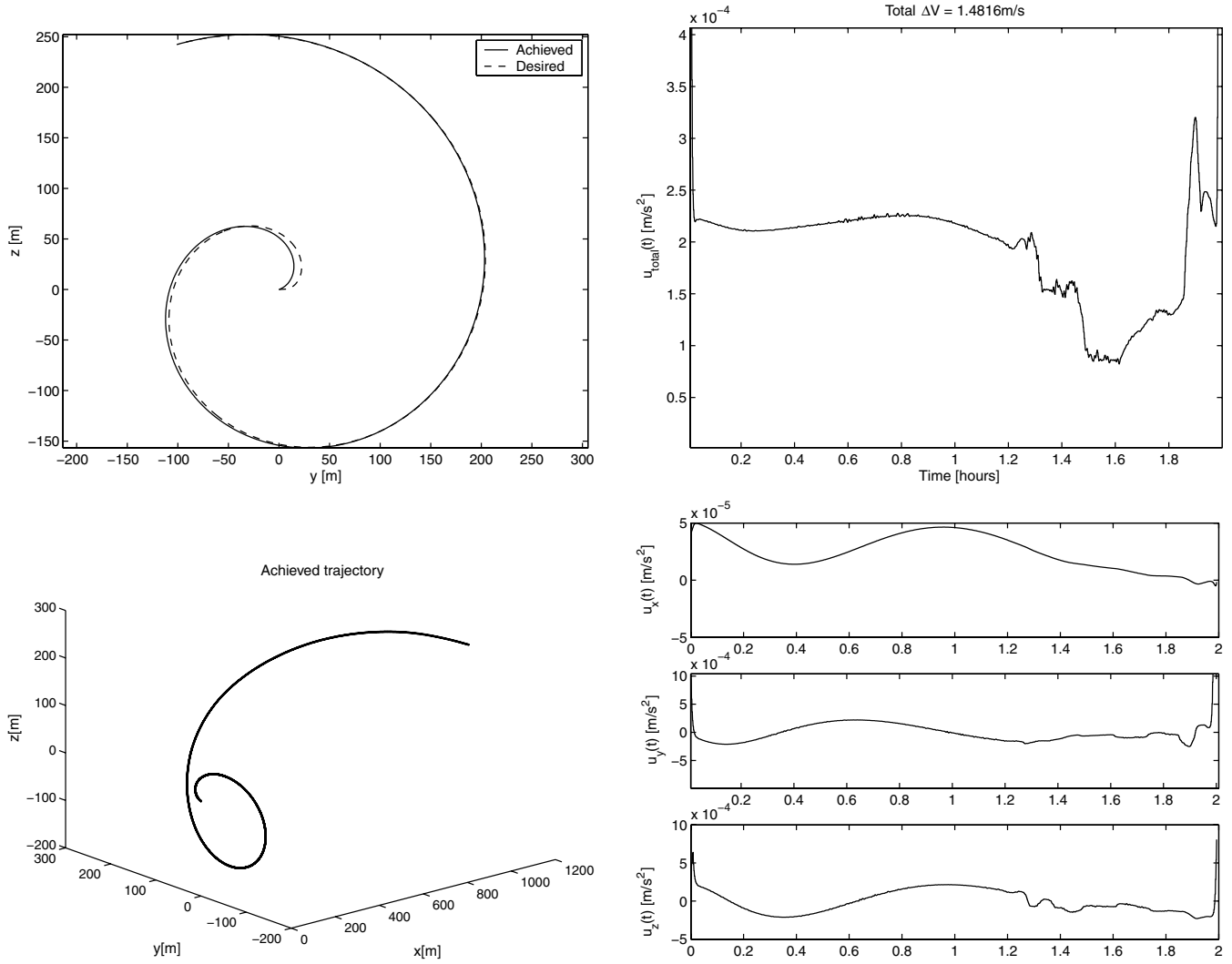


**Fig. 6 An 11-spacecraft, 2 h maneuver, resolution on target = 1 m.**

converges to a solution. Using this algorithm, this first stage of the problem is solved for the parameters of the imaging system and the obtained trajectories are an input for an LQR tracker controller.

For the LQR problem, the dynamic system is

$$\begin{bmatrix} \dot{x} \\ \dot{y} \\ \dot{z} \\ \ddot{x} \\ \ddot{y} \\ \ddot{z} \end{bmatrix} = \begin{bmatrix} 0 & 0 & 0 & 1 & 0 & 0 \\ 0 & 0 & 0 & 0 & 1 & 0 \\ 0 & 0 & 0 & 0 & 0 & 1 \\ 3a^2 & 0 & 0 & 2a & 0 & 0 \\ 0 & -2a & 0 & 0 & 0 & 0 \\ 0 & 0 & -a^2 & 0 & 0 & 0 \end{bmatrix} \begin{bmatrix} x \\ y \\ z \\ \dot{x} \\ \dot{y} \\ \dot{z} \end{bmatrix} + \begin{bmatrix} 0 & 0 & 0 \\ 0 & 0 & 0 \\ 0 & 0 & 0 \\ 1 & 0 & 0 \\ 0 & 1 & 0 \\ 0 & 0 & 1 \end{bmatrix} \begin{bmatrix} u_x \\ u_y \\ u_z \end{bmatrix} \tag{71}$$

and the trajectory to be tracked is

$$r(t) = \begin{bmatrix} y_t(t) \\ z_t(t) \\ \dot{y}_t(t) \\ \dot{z}_t(t) \end{bmatrix} = \begin{bmatrix} r\cos(\theta) \\ r\sin(\theta) \\ k\omega(\cos(\theta) - kr\sin(\theta)) \\ k\omega(\sin(\theta) + kr\cos(\theta)) \end{bmatrix} \tag{72}$$

where $k$ is the expansion rate of the spiral and $\omega$, $r$, and $\theta$ are defined from the NLP solution in the first stage.

Then, the cost function of the LQR optimal control problem is

$$\mathcal{J} = \frac{1}{2}(Cx(T) - r(T))^T P(Cx(T) - r(T)) + \frac{1}{2}\int_{t_o}^{T} (Cx - r)^T Q(Cx - r) + u^T R u \, \mathrm{d}t \tag{73}$$

with

$$C = \begin{bmatrix} 0 & 1 & 0 & 0 & 0 & 0 \\ 0 & 0 & 1 & 0 & 0 & 0 \\ 0 & 0 & 0 & 0 & 1 & 0 \\ 0 & 0 & 0 & 0 & 0 & 1 \end{bmatrix} \tag{74}$$

$P$ being a positive–semidefinite matrix, and $Q$, $R$ being positive–definite matrices. Note that the $x$ direction (optical axis direction) is free, and the spiral is projected on the $y$–$z$ directions of the LVLH coordinate system. Then, the controller

$$u(t) = -R^{-1}B^T S(t)x + R^{-1}B^T v \tag{75}$$

is an optimal control for the desired trajectory, with:

$$-\dot{S} = A^T S + SA - SBR^{-1}B^T S + C^T QC \tag{76}$$

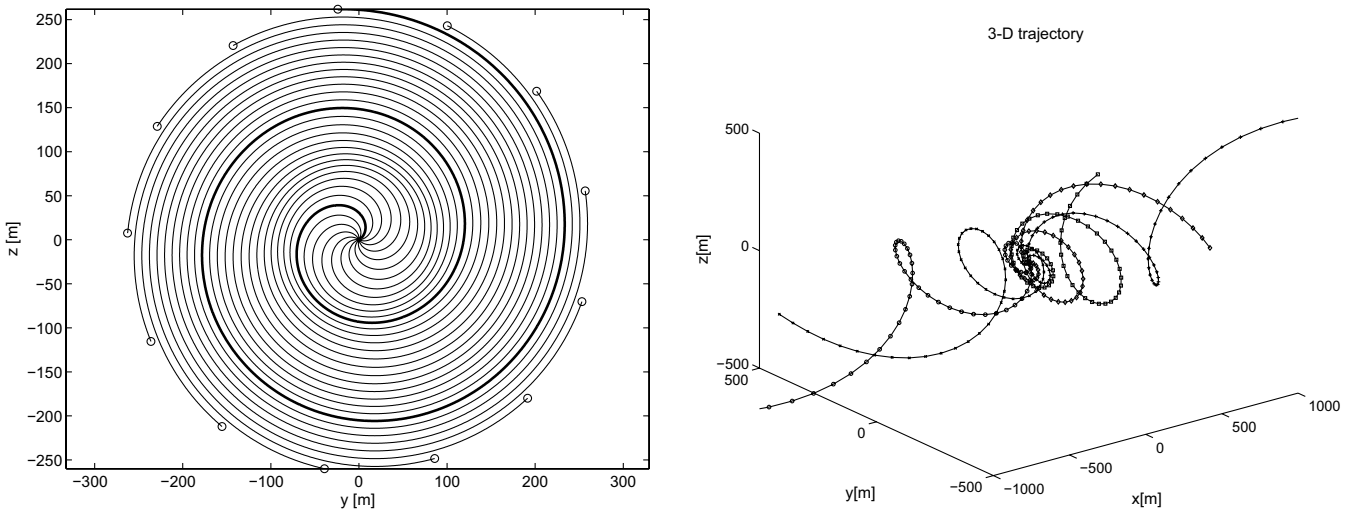


**Fig. 7 A 13-spacecraft, 3 h maneuver, 100 × 100 pix. Left: projected path in the *y*–*z* plane of the 13 spacecraft; right: 3-D trajectories of five of the spacecraft in the LHLV reference frame.**

$$-\dot{v} = (A - BK)^T v + CQr(t) \tag{77}$$

This algorithm accounts for the orbital dynamics and the requirements on acceleration and required thrust, describing the imaging spirals in the desired plane.

Figure 6 shows the results for one of these maneuvers. The trajectory shown is for one of the 13 spacecraft in the maneuver. The projection in the LHLV plane is presented in the top left plot.

Figure 7 displays the trajectories of five out of 13 spacecraft in a 2 h maneuver, and the three-dimensional paths are described. These trajectories do not intersect because the relative angular distance in the projected plane is constant and, thus, the distance between spacecraft is proportional to the radial position in the spiral that is monotonically increasing. The trajectories are not confined to a plane, but they project the optimal trajectories in the perpendicular plane to the optical axis.

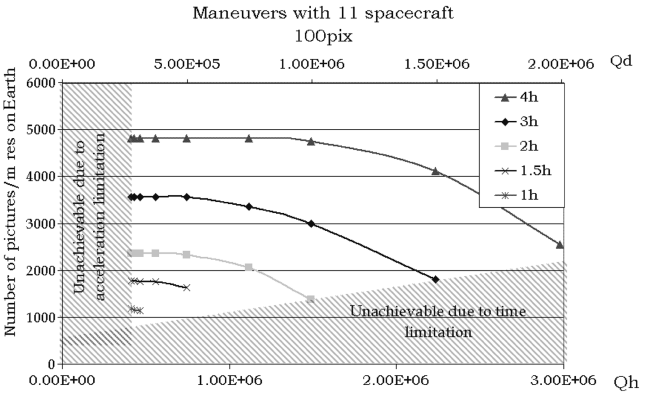


**Fig. 8 An 11-spacecraft maneuver, 100 × 100 pix. Number of images vs quality (*Qd* = directinterferometry, *Qh* = heterodyne interferometry).**

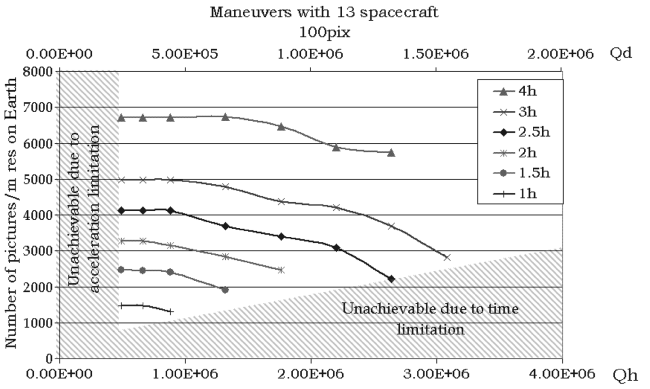


**Fig. 9 A 13-spacecraft maneuver, 100 × 100 pix. Number of images vs quality (*Qd* = directinterferometry, *Qh* = heterodyne interferometry).**

## VI. Results

In this section, the results for the solutions for the optimization problem posed previously are described, and the behavior for selected parameters and different configurations are displayed, to describe the relation between the fuel consumption and the quality of the reconstructed images. The diameter of the maneuver is defined by the desired resolution of the image by the position of the first zero in the interferometric pattern of the Airy disk, which is approximately [1]

$$D = 1.22\frac{\lambda \bar{z}}{\delta} \tag{78}$$

where $\delta$ is the resolution of the image. If the design is calculated for $\lambda = 10\ \mu$m and an approximate resolution of 1 m in the target, the diameter of the optical aperture is about 500 m. The size of the collecting telescopes required to acquire the light from the prescribed area of the target is given by the same criteria [1]. The rate of arrival of photons for imaging a thermally radiating object on Earth can be calculated as [20]

$$\mu_{\text{tot}} = \frac{2c}{\lambda^4(e^{hc/\lambda kT} - 1)}\frac{\eta\xi(\Delta\lambda)2A_{\text{tel}}(\mathrm{d}n_{\text{pix}})^2}{\bar{z}^2}[ph/s] \tag{79}$$

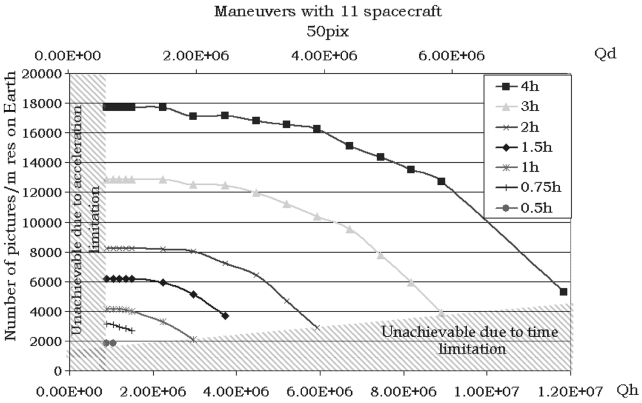


**Fig. 10 An 11-spacecraft maneuver, 50 × 50 pix. Number of images vs quality (*Qd* = directinterferometry, *Qh* = heterodyne interferometry).**

**Table 1 Minimum time and minimum quality given acceleration constraints $a_{\max} = 4.5$ mm/s$^2$**

| | 50 pix | | | 100 pix | | |
|---|---|---|---|---|---|---|
| $M$ | Min time, h | Min $Qd \times 10^5$ | Min $Qh \times 10^5$ | Min time, h | Min $Qd \times 10^5$ | Min $Qh \times 10^5$ |
| 9 | 0.51 | 7.77 | 7.54 | 0.97 | 3.78 | 3.67 |
| 11 | 0.42 | 6.08 | 9.21 | 0.80 | 2.96 | 4.49 |
| 13 | 0.37 | 4.99 | 10.9 | 0.68 | 2.43 | 5.30 |

where $\xi$ is the emissivity coefficient of the radiating body, which can be as low as 0.1; $\eta$ is the absorption coefficient of the atmosphere at the given wavelength; and $A_{\text{tel}}$ is the area of the telescopes. The bandwidth $\Delta\lambda$ is a parameter limited by the desired resolution and the measuring system. In the case of heterodyne interferometry, it is of the order of 2 nm and can be greater in the case of direct interferometric methods [3].

In the case of the thermal source, the term $\bar{\bar{\Delta}}$ in the spiral trajectory optimization [Eq. (10)] is

$$\bar{\bar{\Delta}} = \left(1 + \frac{1-\epsilon}{\tau_{\text{opt}} n_s (e^{h\nu/kT_{\text{opt}}} - 1)}\right) \frac{(M-1)^2 \lambda^4 \bar{z} (e^{hc/\lambda kT} - 1)}{2\tau_{\text{opt}} \varsigma \eta \xi c M (\Delta\lambda) A_{\text{tel}} d_{\text{pix}}^2} Q_d \tag{80}$$

and replacing the size of the preceding telescope,

$$\bar{\bar{\Delta}} = \left(1 + \frac{1-\epsilon}{\tau_{\text{opt}} n_s (e^{h\nu/kT_{opt}} - 1)}\right) \frac{2 n_{\text{pix}}^2 (M-1)^2 \lambda^2 (e^{hc/\lambda kT} - 1)}{\varsigma \eta \xi c M (\Delta\lambda)(1.5\pi)} Q_d \tag{81}$$

Similarly, for heterodyne detection,

$$\bar{\bar{\Delta}} = \left(1 + \frac{1}{n_s} + \frac{1-\epsilon}{n_s (e^{h\nu/kT_{opt}} - 1)}\right) \frac{2 n_{\text{pix}}^2 \lambda^2 (e^{hc/\lambda kT} - 1)}{c M \eta \xi (\Delta\lambda) 1.5\pi} Q_h \tag{82}$$

where $Q$ is the image-quality factor mentioned in the previous section, $n_{\text{pix}}$ is the number of pixels in the image, and $M$ is the number of spacecraft.

Simulations and calculations of fuel consumption for different maneuvers were performed. Figures 6 and 7 show the features of these types of maneuvers. In Fig. 6, the plots show the values for the accelerations in all three axes, as well as the tracking of the trajectories by the inner-loop controller. Notice that the level of

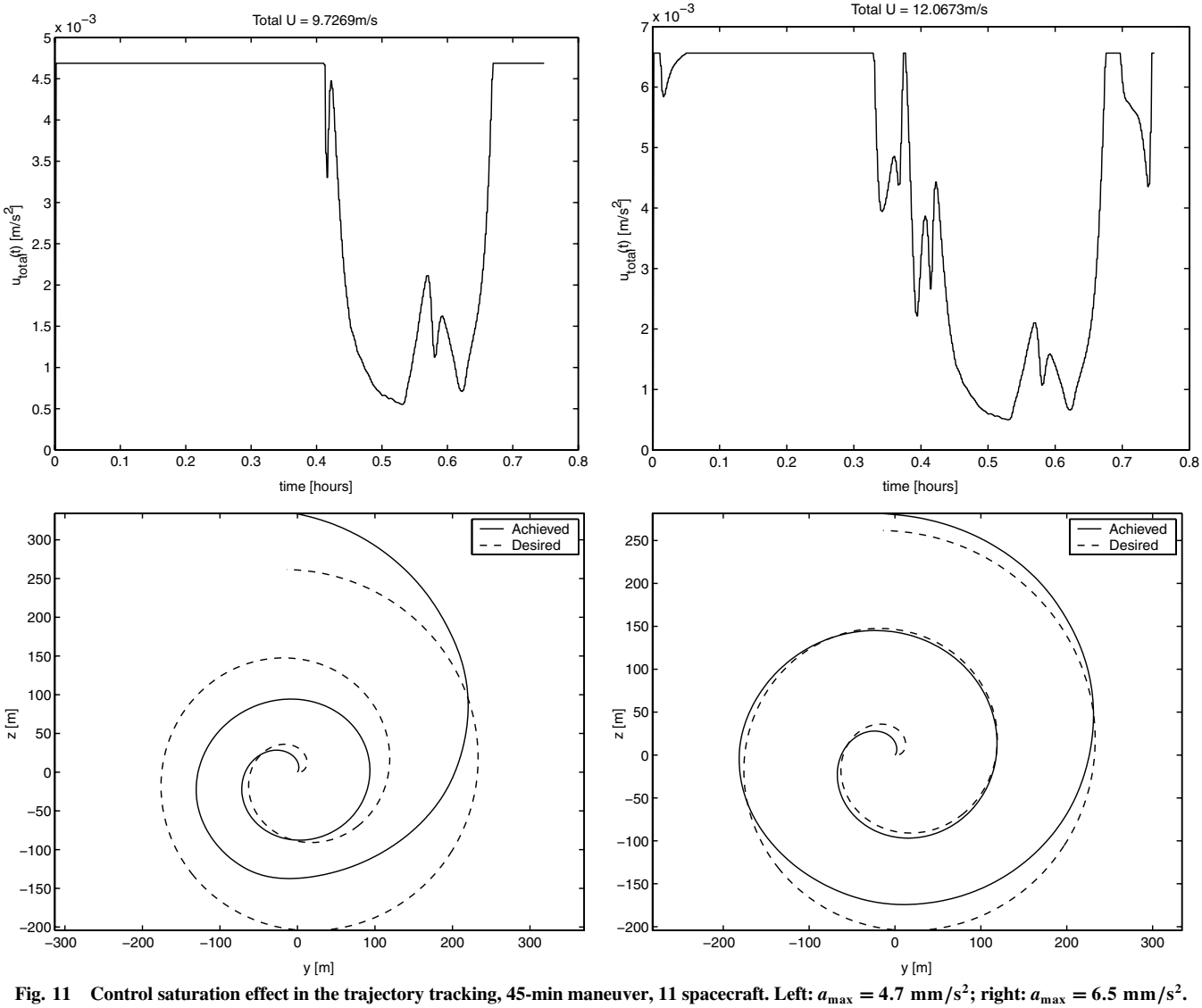


**Fig. 11 Control saturation effect in the trajectory tracking, 45-min maneuver, 11 spacecraft. Left: $a_{\max} = 4.7$ mm/s$^2$; right: $a_{\max} = 6.5$ mm/s$^2$.**

acceleration in the $x$ direction is orders of magnitude smaller than in the other directions. Notice as well that the major discrepancies are at the beginning of the tracking. This behavior can be improved by adjusting the weighting parameters in the LQR controller. In Fig. 7, 5 of the 13 constituent trajectories are shown to illustrate how the three-dimensional trajectories can differ in the $x$–$y$–$z$ plane, but their projection onto the $y$–$z$ plane follows the desired trajectory.

To condense the results for the fuel consumption of different maneuvers, Figs. 8–10 display, for different configurations, the number of missions realizable with the calculated $\Delta V$, assuming an electric propulsion system with a specific impulse of 3500 s, and fixing the maximum ratio of fuel to a total mass at 0.3. It is noted that the number of realizable maneuvers are increased as the quality parameter is relaxed.

Notice, however, that there are two unachievable zones. The first one is due to the fact that there is a limitation in the minimum time of the maneuvers given the available thrust of electric propulsion systems. Given the requirements of power of electric propulsion systems (in the most recent prototypes, the efficiency is 70–80 mN/kW [21] and the presently available power sources with specific power of 200 kW/kg [22]), the maximum acceleration of the system is limited by the fraction of the mass of the spacecraft to be power generation. Assuming a value of 25% for the percentage of the mass to be power generation, the limit in the accelerations of the spacecraft is about 4.5 mm/s$^2$. Given this limiting value, the minimum time of maneuver as well as the minimum value for $\bar{\bar{\Delta}}$ and $Q$ can be calculated from Eqs. (9) and (14) when assuming continuous maximum thrust during the whole maneuver and deep-space dynamics (as a lower boundary):

$$T = \int_{R_{\min}}^{R_{\max}} \frac{\mathrm{d}r}{v_r(r)} \tag{83}$$

$$= \int_{R_{\min}}^{R_{\max}} \frac{\mathrm{d}r}{\sqrt{a_{\max}^2 k^2/\sqrt{r^2+4k^2}}} \tag{84}$$

and

$$\bar{\bar{\Delta}}_{\min} = \sum_{i=1}^{N_R} \alpha_i \beta_i \frac{1}{\sqrt{a_{\max}^2 k^2/\sqrt{1+4k^2}}} \tag{85}$$

The results are shown in Table 1. Notice how the minimum time reduces with the reduction of the resolution requirements and increases with the number of spacecraft. If the acceleration constraint is relaxed, solutions for faster maneuvers are found, but the system is not able to follow them. Figure 11 shows the effect of the saturation of the control in the trajectories for a 45-min, 11-spacecraft maneuver.

On the other side, the maximum value of $Q$, that is, the highest quality achievable, is also constrained by the time of the maneuver; for a given time of maneuver, there is a limit in the minimum velocity, and so this limits the achievable quality. The two unachievable regions are clearly depicted in Figs. 9–11. The optimization problem and the LQR are normalized such that the total cost obtained is directly proportional to the radius of maneuver and, therefore, the number of missions is directly proportional to the resolution on Earth. The number of pixels in the image is also an important factor in the fuel cost. The number of images in Figs. 9–11 are given per meter of resolution desired on the target. The reduction of the number of pixels per image means a less-tight spiral maneuver and consequently less consumption of fuel. This can be noticed in Fig. 11, which is calculated for a $50 \times 50$ pix image.

## VII. Conclusions

In this paper, a method to design fuel-efficient trajectories for multispacecraft interferometric imaging systems is proposed such that they achieve certain image-quality requirements. The results delineate the principal features of multispacecraft interferometric imaging systems in a near-Earth orbit and their imaging capabilities. The method is applied to a GEO-located IR imaging system of Earth-based targets emitting thermal radiation.

Additionally, relationships between the error in the frequency content and the error in the image were defined. Two different measurements of the quality of the image were proposed. One defines the probability that the error in any pixel of the image is within a bound. The other considers the probability that the total error in the image is within a given bound. These probabilities were shown to be related to the maximum error in the frequency content and, consequently, define constraints in the trajectories of the maneuver. Missions intended to do night imaging of thermally radiating sources from a geostationary orbit were considered. The proposed trajectory optimization method was used to compute the fuel consumption for different cases, and the numerical results were used to relate the fuel requirements and the quality of the images. It was seen that the fuel consumption of these systems increases with the number of pixels (i.e., resolution) in the desired image and, therefore, is reduced with the increase in the size of the light collectors. A larger number of collectors reduces the fuel consumption, although it was seen that longer maneuvers require less fuel too.

The propulsion systems and the size of the collecting antennas define operational limits in this type of system. The numerical values found for the fuel and power requirements indicate the feasibility of such a system, given the current state of the art in these areas. However, the actual realization of such a system will require the study of accurate pointing capabilities of the light collectors and efficient spacecraft power sources to achieve better images in shorter durations.

## References


[1] Quirrenbach, A., "Optical Interferometry," *Annual Review in Astronomy and Astrophysics*, Vol. 39, 2001, pp. 353–401.

[2] Goodman, J. W., *Introduction to Fourier Optics*, McGraw–Hill, Boston, MA, 1996.

[3] Townes, C. H., "Spatial Interferometry in the Mid-Infrared Region," *Journal of Astrophysics and Astronomy*, Vol. 5, No. 2, 1984, pp. 111–130.
doi:10.1007/BF02714984

[4] Chakravorty, S., "Design and Optimal Control of Multi-Spacecraft Interferometric Imaging Systems," Ph.D. Thesis, Department of Aerospace Engineering, University of Michigan, Ann Arbor, MI, 2004.

[5] Hussein, I. I., Scheeres, D., and Hyland, D. C., "Interferometric Observatories in Earth Orbit," *Journal of Guidance, Control, and Dynamics*, Vol. 27, No. 2, 2004, pp. 297–301.

[6] Hyland, D. C., "Entry Pupil Processing Approaches for Exo-Planet Imaging," *Proceedings of SPIE—The International Society for Optical Engineering*, Vol. 5905, SPIE–International Society for Optical Engineering, Bellingham, WA, 2005, p. 18.

[7] Hyland, D. C., "Constellations Using Entry Pupil Processing for High Resolution Imaging of Geosynchronous Objects," *Proceedings of the 16th AAS/AIAA Space Flight Mechanics Conference*; also AAS Paper 06-230, 2006, pp. 1–18.

[8] Hyland, D. C., "Exo-Planet Detection via Stellar Correlation Interferometry," *Proceedings of SPIE—The International Society for Optical Engineering*, Vol. 5905, SPIE–International Society for Optical Engineering, Bellingham, WA, 2005, pp. 1–17.

[9] Scharf, D. P., Hadaegh, F. Y., and Ploen, S. R., "A Survey of Spacecraft Formation Flying Guidance and Control. Part II: Control," *Proceedings of the 2004 American Control Conference*, Vol. 4, No. 4, IEEE Publications, Piscataway, NJ, June 2004, pp. 2976–2985.

[10] Kong, E. M., Miller, D. W., and Sedwick, R, J., "Exploiting Orbital Dynamics for Aperture Synthesis Using Distributed Satellite Systems: Applications to Visible Earth Imager System," *Journal of the Astronautical Sciences*, Vol. 47, Nos. 1–2, 1999, pp. 53–75.

[11] DeCoe, A. B., "Orbital Station-Keeping for Multiple Spacecraft Interferometry," *Journal of the Astronautical Sciences*, Vol. 39, No. 3, 1991, pp. 283–297.

[12] Chakravorty, S., Kabamba, P. T., and Hyland, D. C., "Guaranteed Classification Performance of Multi-Spacecraft Interferometric Imaging Systems," *Journal of the Astronautical Sciences*, Vol. 51, No. 2, April–June 2003, pp. 205–226.

[13] Chakravorty, S., Kabamba, P. T., and Hyland, D. C., "Design of Minimum Time Maneuvers for Multi-Spacecraft Interferometric

Imaging Systems," *Proceedings of the SPIE, Modeling and Systems Engineering for Astronomy*, Vol. 5497, SPIE–International Society for Optical Engineering, Bellingham, WA, 2004, pp. 427–436.

[14] Chakravorty, S., Kabamba, P. T., and Hyland, D. C., "Design of Minimum Time Maneuvers for Multi-Spacecraft Interferometric Imaging Systems," *Journal of the Astronautical Sciences*, Vol. 52, No. 3, July–Sept. 2004, pp. 301–329.

[15] Chakravorty, S., "On the Fuel Optimality of Maneuvers for Multispacecraft Interferometric Imaging Systems," AAS Paper 05-159, 2005.

[16] Ramirez, J., and Chakravorty, S., "Fuel Optimal Spiral Maneuvers for Multispacecraft Interferometric Imaging Systems in Deep Space," AAS Paper 06-164, 2006.

[17] Chakravorty, S., Kabamba, P. T., Hyland, D. C., "Modeling of Image Formation in Multi-Spacecraft Interferometric Imaging Systems," *AIAA Space 2004 Conference and Exposition*, Vol. 1, AIAA, Reston, VA, 2004, pp. 699–720.

[18] Ramirez, J., "Design of Fuel Optimal Maneuvers for Multispacecraft Interferometric Imaging Systems," Master's Thesis, Texas A&M University, June 2006.

[19] Chakravorty, S., and Ramirez, J., "On the Fuel Optimal of Multispacecraft Interferometric Imaging Systems," *Journal of Guidance, Control, and Dynamics*, Vol. 30, No. 1, 2007, pp. 227–236. doi:10.2514/1.20178

[20] Siegel, R., and Howell, J., *Thermal Radiation and Heat Transfer*, 4th ed., Taylor and Francis, London, 2002, pp. 13–145.

[21] Janosky, R., and Tverdokhlebov, S., "High Power Hall Thrusters," NASA TM-1999-209436, 1999; also AIAA Paper 99-2949, 1999.

[22] Fortescue, P., Stark, J., and Swinerd, G., *Spacecraft Systems Engineering*, Wiley, New York, 2003, pp. 170–210.